

Rapid Radiation Belt Losses Occurring During High-Speed Solar Wind Stream–Driven Storms: Importance of Energetic Electron Precipitation

Aaron T. Hendry,¹ Craig J. Rodger,¹ Mark A. Clilverd,² Neil R. Thomson,¹ Steven K. Morley,³ and Tero Raita⁴

Recent studies have shown how trapped energetic radiation belt electron fluxes rapidly “drop out” during small geomagnetic disturbances triggered by the arrival of a solar wind stream interface (SWSI). In the current study, we use satellite and ground-based observations to describe the significance of energetic electron precipitation (EEP) and direct magnetopause shadowing loss mechanisms, both of which have been suggested as possible causes of the dropouts. Superposed epoch analysis of low-Earth-orbiting Polar-Orbiting Environmental Satellites (POES) spacecraft observations indicate that neither “classic” magnetopause shadowing nor EEP appear able to explain the dropouts. However, SWSI-triggered dropouts in trapped flux are followed ~ 3 h later by large increases of EEP, which start as the trapped electron fluxes begin to recover and may be signatures of the acceleration process, which rebuilds the trapped fluxes. Ground-based observations indicate typical >30 keV EEP flux magnitudes of $\sim 8 \times 10^5$ electrons $\text{cm}^{-2} \text{sr}^{-1} \text{s}^{-1}$. While these are ~ 10 times larger than the equivalent precipitating fluxes measured by POES, this is consistent with the small viewing window of the POES telescopes.

1. INTRODUCTION

The basic structure of the Van Allen radiation belts was recognized from shortly after their discovery following the International Geophysical Year [*Van Allen and Frank*, 1959; *Hess*, 1968]. Despite being discovered at the dawn of the space age, there are still fundamental questions concerning the acceleration and loss of highly energetic radiation belt electrons [*Thorne*, 2010]; energetic electron fluxes can increase or decrease by several orders of magnitude on timescales of less

than a day. The coupling of the Van Allen radiation belts to the Earth’s atmosphere through precipitating particles is an area of intense scientific interest, principally due to two differing research activities. One of these concerns the physics of the radiation belts and primarily the evolution of energetic electron fluxes during and after geomagnetic storms [e.g., *Reeves et al.*, 2003]. The other focuses on the response of the atmosphere to precipitating particles, with a possible linkage to climate variability [e.g., *Turunen et al.*, 2009; *Seppälä et al.*, 2009]. Both scientific areas require increased understanding of the nature of the precipitation, particularly as to the precipitation drivers, as well as the variation of the fluxes and energy spectrum for electrons lost from the outer radiation belts. One area of interest has been the link between the weak geomagnetic storms triggered by the arrival of a high-speed solar wind stream interface (SWSI) and associated “dropouts” in energetic electron fluxes [e.g., *O’Brien et al.*, 2001; *Miyoshi and Kataoka*, 2008; *Morley et al.*, 2010a]. These events highlight the dynamic nature of the outer radiation belt electron fluxes and are the subject of a review in the current monograph [*Turner et al.*, this volume].

The combination of observations from a large number of spacecraft provides a much higher time resolution than

¹Department of Physics, University of Otago, Dunedin, New Zealand.

²British Antarctic Survey, Cambridge, UK.

³Los Alamos National Laboratory, Los Alamos, New Mexico, USA.

⁴Sodankylä Geophysical Observatory, University of Oulu, Sodankylä, Finland.

possible from a single spacecraft, and this has recently provided new understanding into the SWSI-linked dropout events. A statistical study utilizing nine GPS-borne particle detectors and superposed epoch analysis (SEA) around the arrival of 67 SWSIs showed a strong repeatable “signal” of a rapid electron flux dropout [Morley *et al.*, 2010b]. Dropouts occurred in a median time scale of ~ 7 h, with median electron counts falling by 0.4–1.8 orders of magnitude for all L^* (where L^* is a magnetic drift invariant) [Roederer, 1970]. The SWSI triggered geomagnetic storms with small Dst excursions (-40 nT) and small Kp increases ($Kp \approx 4$). Indeed, while these events show a storm-like evolution in Dst and Kp , the majority have maximum Dst excursions less than -30 nT and thus are not storms by the “traditional” definitions [e.g., Loewe and Pröls, 1997], although we will refer to them as such for want of a better label. The storms started ~ 6 h before the epoch defined by the expected arrival of the SWSI at the Earth’s bow shock nose. While the radiation belt dropouts and recoveries depended on both L^* and energy, only 3 of 67 SWSIs did not have an associated dropout in the electron data.

In the current study, we reconsider satellite and ground-based observations to describe the significance of energetic electron precipitation (EEP) during SWSI-driven geomagnetic storms. We make use of the Morley *et al.* [2010b] epochs to allow “like with like” comparisons with the earlier GPS study. Here we show that the EEP occurs well after the dropout has started and confirm the EEP energy dependence reported earlier. From the existing literature, it appears possible that the dropout is caused by magnetopause shadowing. However, this study shows that the SWSI also triggers a geomagnetic storm some hours after the dropout, which enhances wave-particle interactions leading to EEP, as well as the recovery and enhancement of the trapped electron fluxes. We go on to use ground-based EEP observations to determine the likely precipitation flux into the atmosphere. SWSI-driven events are highly repeatable in form and lead to order of magnitude enhancements in EEP up to very high L shells. As such, the EEP will couple efficiently into the polar vortex and may influence the chemistry and dynamics of the polar neutral atmosphere. Recent work has demonstrated that geomagnetic storms produce levels of EEP that are significant in the lower ionosphere [e.g., Rodger *et al.*, 2007] and can significantly alter mesospheric neutral chemistry [Newnham *et al.*, 2011].

2. POES OBSERVATIONS

2.1. SWSI Event Epochs

As noted above, we make use of the epochs given by Morley *et al.* [2010b, Table A.1]. The experimental data we

use in this study, Polar-Orbiting Environmental Satellites (POES) electron counts and subionospheric VLF propagation, are both strongly affected by high-energy protons, which are likely to dominate over any electron response. We, therefore, removed two of the Morley epochs (7 May 2005 and 28 July 2005) from our list as these occurred in the declining phase of solar proton events. We, therefore, have 65 epochs in total from Table 2 of Morley *et al.* [2010b].

In our investigation of the POES spacecraft data described below, we follow the approach of earlier authors and undertake SEA. We explicitly follow the approach of Morley *et al.* [2010b].

2.2. POES SEM-2 Observations

We make use of measurements from the Space Environment Monitor (SEM-2) instrument package onboard the POES, which are in Sun-synchronous orbits at ~ 800 – 850 km altitudes. SEM-2 includes the Medium Energy Proton and Electron Detector (MEPED). For a detailed description of the SEM-2 instruments, see the works of Evans and Greer [2004]. We use SEM-2 observations from the NOAA-15 through 19 satellites plus the METOP-2 satellite, which also carries an SEM-2. All POES data is available from <http://poes.ngdc.noaa.gov/data/> with the full-resolution data having 2 s time resolution. NOAA has developed new techniques to remove the significant low-energy proton contamination from the POES SEM-2 electron observations [e.g., Rodger *et al.*, 2010a], which has been described in Appendix A of Lam *et al.* [2010]. This algorithm is available for download through the Virtual Radiation Belt Observatory (<http://virbo.org>).

The SEM-2 detectors include integral electron telescopes with energies of >30 keV (e1), >100 keV (e2), and >300 keV (e3), pointed in two directions. Modeling work has established that the 0° telescopes monitor particles in the atmospheric bounce loss cone that will enter the Earth’s atmosphere below the satellite when the spacecraft is poleward of $L < 1.5$ – 1.6 [Rodger *et al.*, 2010b, Appendix A]. Note however, that the 0° telescopes only observe a fraction of the bounce loss cone even when they are directed such that they only measure bounce loss cone fluxes; building on the Rodger *et al.* [2010b] modeling, we find that, in practice, at best 10% of the total bounce loss cone area is sampled, a value that can drop to less than $\sim 2.5\%$ depending on the location. In contrast, the 90° directed MEPED telescope tends to detect electrons with higher pitch angles, i.e., the drift loss cone and trapped electron populations. In practice, once even a small fraction of trapped electron fluxes are visible to the instrument, these will strongly dominate over any fluxes inside a loss cone. This occurs from roughly $L = 4$ – 5 and above, depending on the location.

In addition to the electron telescopes, the MEPED instrument also includes a number of proton telescopes. The SEM-2 proton detectors also suffer from contamination, falsely responding to electrons with relativistic energies, which can be useful for radiation belt studies [e.g., Sandanger *et al.*, 2007; Yando *et al.*, 2011] outside of solar proton events when significant energetic proton fluxes are present. In particular, the P6 telescope detectors, which are designed to measure >6.9 MeV protons, also respond to either trapped or bounce loss electrons (depending on L shell) with energies in the relativistic range [Yando *et al.*, 2011]. As shown in Figure 8 of Yando *et al.* [2011], the P6 channel plays a complementary role to the e1–e3 channels for detection of relativistic electrons and is sensitive to electrons of energy larger than roughly 1000 keV.

2.3. Superposed Epoch Analysis of MEPED Electrons

Before undertaking SEA, we first combine the POES-reported particle fluxes varying with L and time, using $0.25 L$ and 1 h time resolution. Observations from inside and around the South Atlantic Magnetic Anomaly are excluded before the measurements are combined. From this dataset, SEA is undertaken using the 65 epochs from Morley *et al.* [2010b]; in addition, another SEA is undertaken with a set of 65 epochs, which are randomly selected from the period January 2004 to December 2008, after having been filtered for solar proton events. This allows an additional check of the significance of any changes observed in the Morley epoch SEA.

2.3.1. POES observations of trapped flux changes. Figure 1 shows the results of this analysis on the 90° directed telescopes, i.e., those primarily showing the effect of SWSI on trapped fluxes. The left-hand panels show the results of analysis using the Morley epochs, while the right-hand side are for the random epochs. The upper panels are the integral flux observations from the >100 keV 90° telescope, the middle panels show the relativistic electron flux variation from the P6 90° telescope, and the lower panels the differential proton flux at 346 keV from the P3 90° telescope.

As a guide, all of the left-hand panels include the result of the SEA applied to GOES >600 keV trapped flux observations for the Morley epochs (green line). The SEA of the >600 keV trapped electrons from geostationary orbits at $L \approx 6.6$ shows a very similar timing to the dropouts in trapped electron fluxes from the GPS spacecraft, which were also made near the geomagnetic equator (i.e., around geostationary orbit). The GOES SEA has been scaled and shifted to fit on this plot, but involves a flux drop of ~ 1.5 orders of magnitude, with a recovery to a flux level that is $\sim 50\%$ larger

than the initial levels. The rapid dropout starts at -0.7 day (relative to the epoch time), reaching the deepest point at $+0.2$ day, with the fluxes having returned to the same level by about $+1$ day.

The POES data shown in Figure 1 indicates that the observations of the trapped electrons and protons near the bottom of the geomagnetic field lines are very different from that near the geomagnetic equator and different from one another. While there is some evidence for a dropout in the >100 keV electrons, this is only true for L greater than about 6 and starts just around the zero epoch. The >300 keV 90° electron fluxes also include some evidence of a dropout (from L greater than about 5.5; not shown, although similar plots have been produced by Miyoshi and Kataoka [2008, Figure 3]), while the >30 keV 90° do not show a clear dropout (not shown). The relativistic electron observations provided by the P6 90° telescope do show a dropout, but this seems to start well after the dropout occurring near the geomagnetic equator. In contrast to all of the electron observations, the trapped differential 346 keV proton fluxes from P3 increase around the time the dropout begins in the electron fluxes near the geomagnetic equator. The same behavior is seen in the 90° directed P1, P2, and P4 detectors (not shown). The significance of the variation shown in the left-hand panels is particularly clear when contrasted for the random epoch SEA results presented in the right-hand panels.

In order to clarify the differences between the electron responses, Figure 2 presents line plots of the changing 90° electron observations from the >100 keV and P6 telescopes at $L = 5.4$. Following the format of Morley *et al.* [2010b], we show the superposed epoch median of the quantity by a black line. The 95% confidence interval for the median is given by the dark gray band. The inner bands mark the interquartile range (medium gray) and the 95% confidence interval about it (light gray). Figure 2 demonstrates the strong differences between the responses of the >100 keV electrons and the relativistic electrons from the P6 channel. During the quiet period before the start of the SWSI-triggered geomagnetic storm, the >100 keV trapped electron fluxes steadily drop. This is reversed at the zero epoch, very close to the time when the electron flux dropouts observed near the geomagnetic equator by GOES and GPS reach their “deepest” extent. In contrast to the >100 keV trapped fluxes, the relativistic electrons exhibit a well-defined dropout, which starts around the same time as seen in the GOES SEA, recovers after 1–1.5 days, and climbs to a slightly higher flux level.

2.3.2. POES observations of precipitating flux changes. Figure 3 shows SEA applied to two of the 0° directed

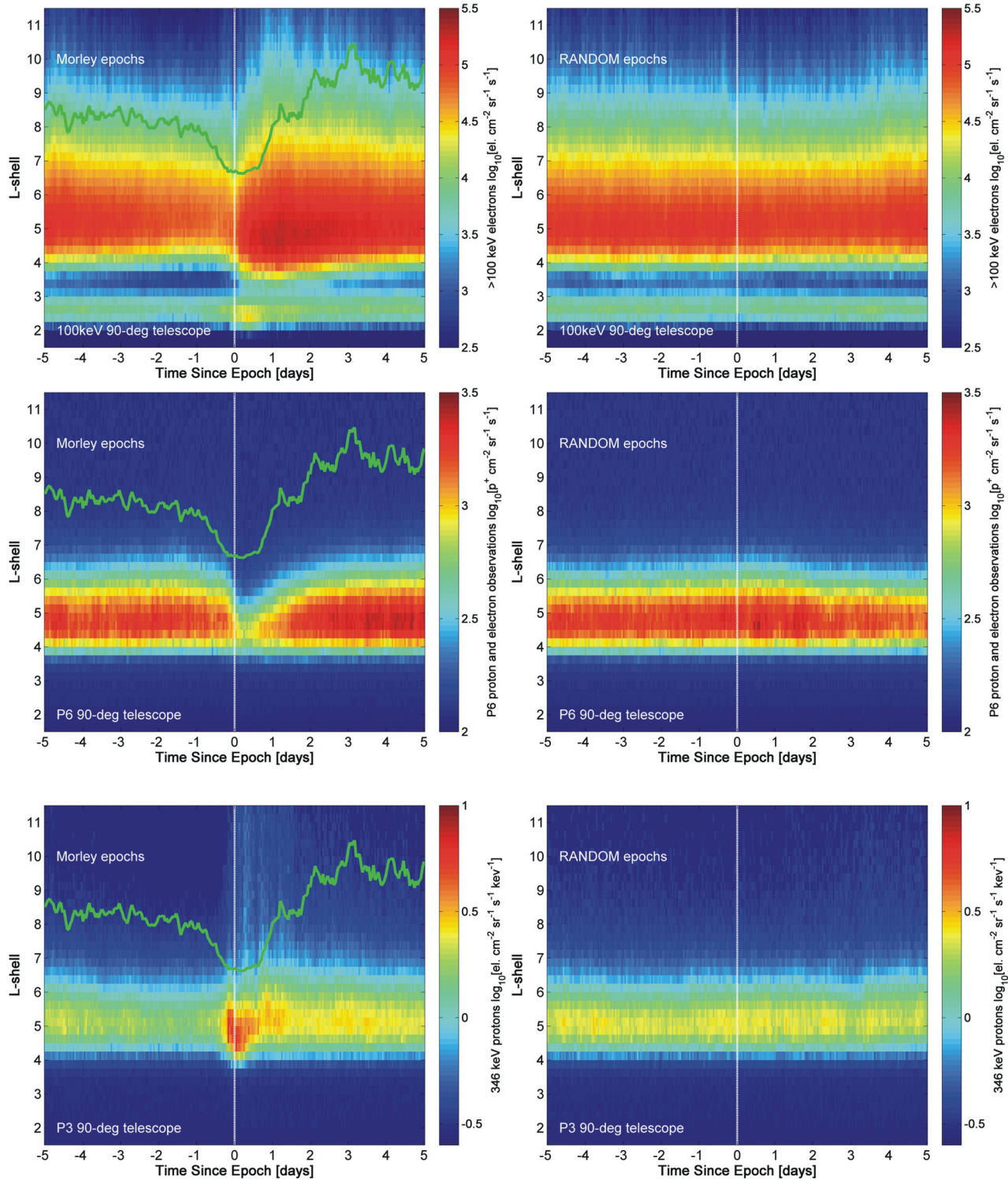


Figure 1. Superposed epoch analysis (SEA) undertaken using the Polar-Orbiting Environmental Satellites (POES) Medium Energy Proton and Electron Detector (MEPED) data. (left) Analysis applied to 65 of the *Morley et al.* [2010b] epochs. (right) A set of random epochs. (top) The integral flux observations from the >100 keV 90° telescope. (middle) Counts from the P6 90° telescope (which responds to relativistic electrons). (bottom) Differential proton flux at 346 keV from the P3 90° telescope. As a guide to the eye, all of the left-hand panels have the result of the Morley SEA applied to GOES >600 keV trapped flux observations (green line).

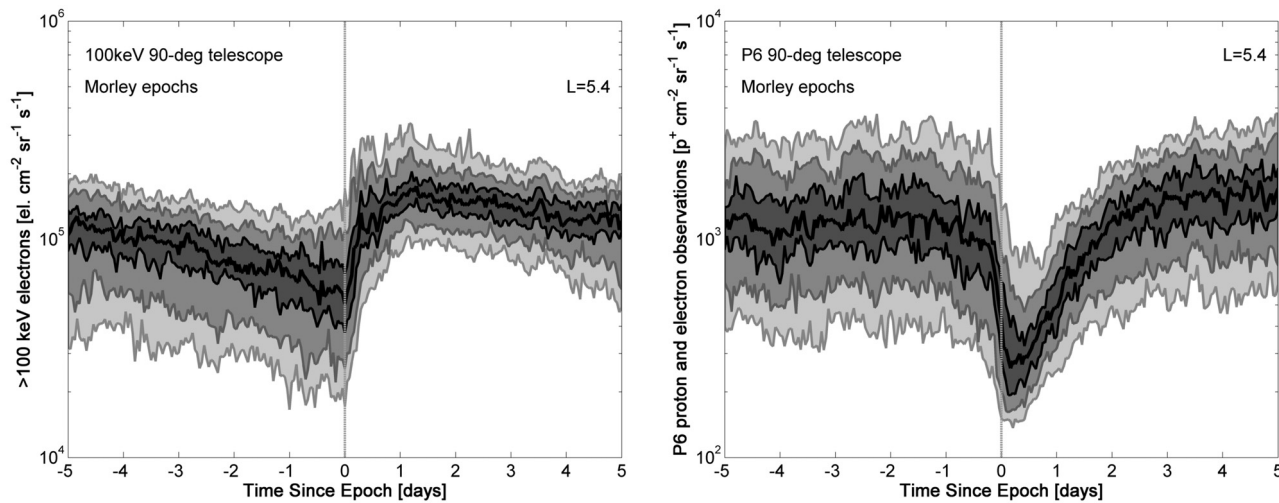


Figure 2. SEA of the POES 90° telescope >100 keV and P6-measured relativistic trapped electron fluxes at $L = 5.4$. The superposed epoch median of the quantity is given by a black line. The 95% confidence interval for the median is given by the dark gray band. The medium gray bands mark the interquartile range and the 95% confidence interval about it (light gray).

telescopes, i.e., those telescopes that detect a portion of the electrons that precipitate into the atmosphere. The format of Figure 3 is otherwise the same as Figure 1. The top panels of this figure show the variation of the >100 keV 0° telescope. By comparison with the random epoch analysis shown on the right-hand side, it is apparent that 4–5 days before the SWSI arrives, the magnitude of >100 keV precipitation is “normal” and then steadily decreases by ~ 0.5 order. This is likely to be linked to the “calm before the storm,” intervals of unusually calm geomagnetic activity, which have been previously reported [e.g., *Clilverd et al.*, 1993]. Very shortly before the zero epoch, the >100 keV flux begins to increase by nearly 2 orders of magnitude (but only slightly more than 1 order of magnitude larger than normal conditions). This peak of precipitation is $\sim +0.3$ days after the zero epoch, around the time the GPS- and GOES-observed electron dropouts are at their deepest. The most significant EEP stretches from $L = 5$ to $L = 8.5$, although there is a clear increase to at least $L = 14$. The EEP decays slowly over the 5 days after the epoch to roughly normal levels. Similar patterns occur with the >30 and >300 keV EEP (not shown) [*Meredith et al.*, 2011, Figure 1]. In contrast, however, the relativistic electron flux from the 0° P6 telescope does not display a decrease before the SWSI arrives (i.e., no “calm” in relativistic EEP) and exhibits a small decrease in precipitation magnitude during the peak timing of the >100 keV EEP, lasting perhaps 1–2 days.

3. CONSISTENCY WITH LOSS MECHANISMS

As noted in the introduction, the existing literature has identified three possible causal mechanisms to explain the GPS-

observed dropout in trapped electron fluxes: (1) magnetopause shadowing, (2) EEP into the atmosphere due to wave-particle interactions, and (3) outward diffusion through the magnetopause. The POES SEA described in the previous section allows us to make conclusions as to the validity of the first two of these loss mechanisms. Note that the monograph in which this paper appears also contains a review covering the major loss mechanisms associated with dropouts [*Turner et al.*, this volume].

3.1. Mechanism 1: Magnetopause Shadowing

As previously noted by *Morley et al.* [2010a], our existing understanding is that the loss timescales possible from the EEP or outward diffusion are not fast enough to explain the dropouts as observed. As such, magnetopause shadowing, sometimes termed “magnetopause encounters” may appear the more likely candidate. This mechanism involves radiation belt particles drifting around the Earth, encountering the magnetopause boundary and being swept away by the solar wind and permanently lost. Characteristics of particle losses by magnetopause shadowing are (1) pitch angle independence of losses of particles on a given drift shell, such that losses would be expected for both high pitch angle particles, which spend most of their time near the geomagnetic equator, and low pitch angle particles, which mirror near the top of the atmosphere and (2) independence of particle charge, mass, or energy, such that electrons or protons that are drifting around the Earth on the same L shell (but in opposite directions) will encounter the magnetopause and, hence, be lost.

On this basis, one would expect the dropouts of electrons observed in the trapped electron fluxes near the geomagnetic

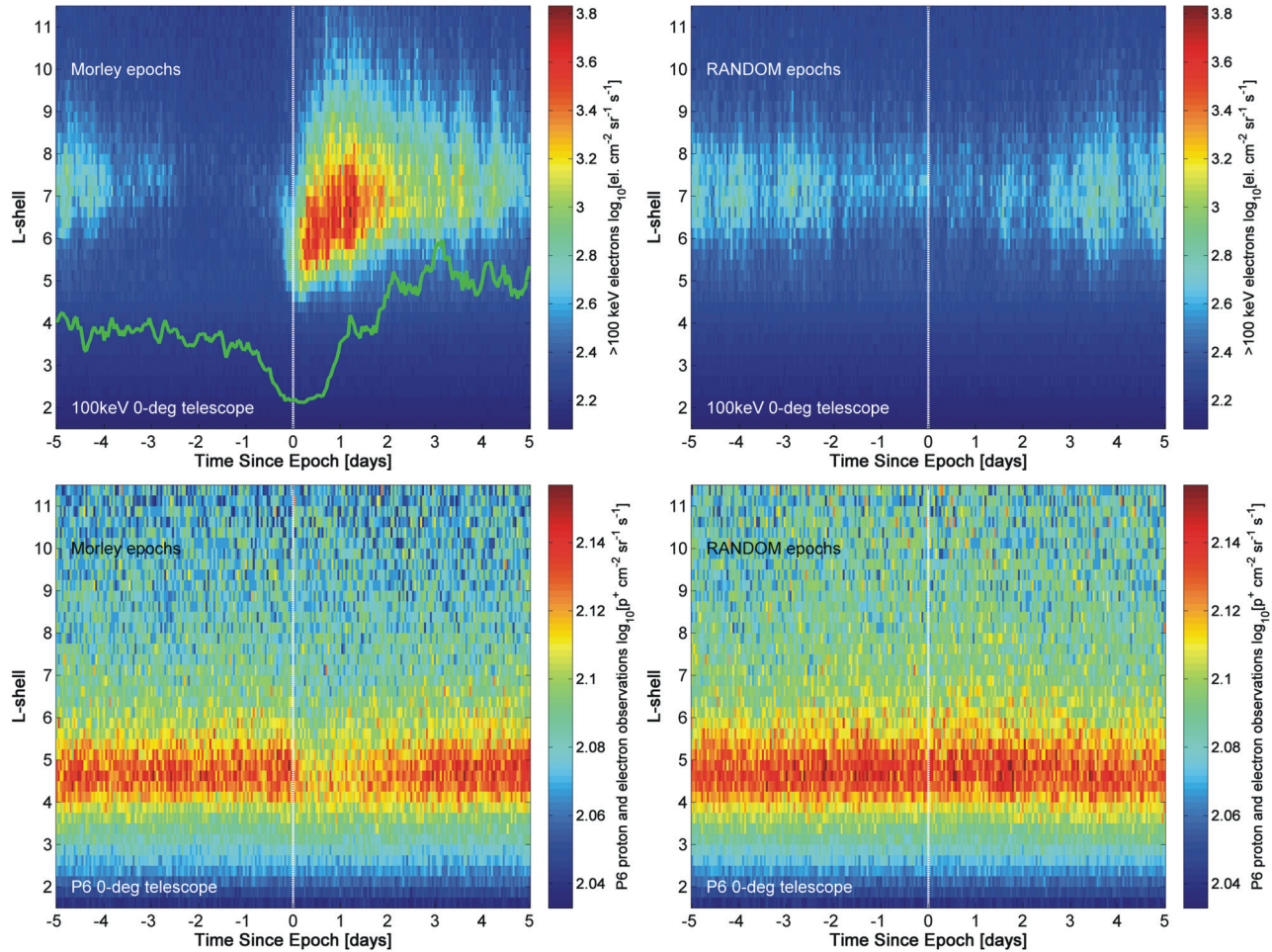


Figure 3. SEA of 0° directed MEPED telescopes in the same format as Figure 1. (top) Integral flux observations from the >100 keV 0° telescope. (bottom) Counts from the P6 0° telescope (which responds to relativistic electrons).

equator by the GPS spacecraft to also be seen in both the trapped electron and proton fluxes measured by the POES low-Earth-orbiting spacecraft. As reported in section 2.3.1, neither of these conditions hold, as the >30 and >100 keV trapped electron fluxes do not show the dropouts reported by satellites near the geomagnetic equator. In addition, the trapped proton fluxes increase rather than decrease during the dropouts. This suggests that direct magnetopause encounters cannot be used to explain the electron flux dropouts. Note that a similar argument was previously employed by *Green et al.* [2004] who contrasted the observed losses of protons and electrons to exclude magnetopause encounters as the dominant loss mechanism.

3.2. Mechanism 2: EEP Into the Atmosphere

As shown in Figure 3 and discussed in section 2 above, the >30 , >100 , and >300 keV 0° electron telescopes (which

measure part of the bounce loss cone) do show significant increases in EEP, but starting at the point that the dropout is at its deepest point and beginning to recover. In contrast, the relativistic electron fluxes measured by the P6 0° telescope show a small decrease in EEP at the same time. Clearly, these observations are not consistent with EEP as the primary mechanism to explain the dropouts. Indeed, it is possible that the opposite is true, that the EEP is the signature of wave-particle-driven acceleration processes, which serve to reverse the electron flux dropouts [e.g., *Thorne*, 2010, and references within].

4. AARDDVARK OBSERVATIONS

Subionospheric VLF propagation detects precipitation due to changes in the ionization number density at altitudes around the lower D region boundary. As the VLF waves

propagate beneath the ionosphere in the Earth-ionosphere waveguide, the EEP-induced ionization produces changes in the received amplitude and phase. Owing to the low attenuation of VLF subionospheric propagation, the EEP-modified ionospheric region may be far from the transmitter or the receiver. As the received subionospheric amplitude is the sum of multiple propagation modes, the response to changes in the waveguide is often complex, and both increases and decreases in amplitude are possible when increased ionization occurs in the waveguide (see, for example, Figure 4 of *Rodger et al.* [2012]). The response also depends on the solar zenith angle along the path. As a result of these factors, subionospheric VLF is not particularly suitable for analysis through superposed epoch. We have, therefore, checked individual paths for a set of specific events to confirm the occurrence of significant EEP.

In this study, we make use of narrow-band subionospheric VLF data received at Churchill (CHUR, 58.75°N, 265.1°E, $L = 7.6$) and Sodankylä, Finland (SGO, 67.4°N, 26.4°E, $L = 5.3$). Both these receivers are part of the Antarctic-Arctic Radiation-belt Dynamic Deposition VLF Atmospheric Research Konsortia (AARDDVARK) [*Cilverd et al.*, 2009]. While the AARDDVARK observations have subsecond time resolution, we will restrict ourselves to 1 min median values to describe the overall transmitter operations. Figure 4 shows the transmitter-receiver great circle paths (GCP), which have been monitored by the Churchill and Sodankylä receivers for at least some part of the time period considered.

The AARDDVARK data was manually examined for evidence of EEP around the time of the Morley epochs. The process was as follows: for each Morley epoch, AARDDVARK data plots were made for all the transmitters monitored by the Churchill and Sodankylä receivers. Data for 4 days both before and after the epoch day were plotted. The days before the epoch were included primarily to construct a quiet-day curve (QDC) to provide comparisons with the epoch day. POES observations show that EEP levels are low immediately before the SWSI epoch, which should allow a good AARDDVARK QDC to contrast with the epoch day. Figure 5 shows examples of the data examined in this way. The upper panel of this figure presents the received amplitude of the GVT 22.1 kHz transmitter received at Sodankylä ($2.5 < L < 5.3$) around the Morley epoch at 06:30 UT on 28 May 2008. Observations on the days before the epoch day are plotted in gray, the epoch day in black. At this time of year, most of the GVT-SGO GCP is sunlit throughout the day, although the transmitter end of the path will have a nighttime ionosphere from ~20 to 04 UT. In general, subionospheric VLF propagation is more sensitive to EEP for nighttime rather than daytime ionospheric conditions [*Rodger et al.*, 2012], due to the extremely large D region energy input from the Sun during the day. On this day, there is a very clear precipitation-induced decrease in the received amplitude starting about 1 h after the epoch (the epoch being marked by the vertical line) continuing through to ~11 UT where the amplitude clearly returns to the QDC defined by the previous days. In this time, the amplitude initially

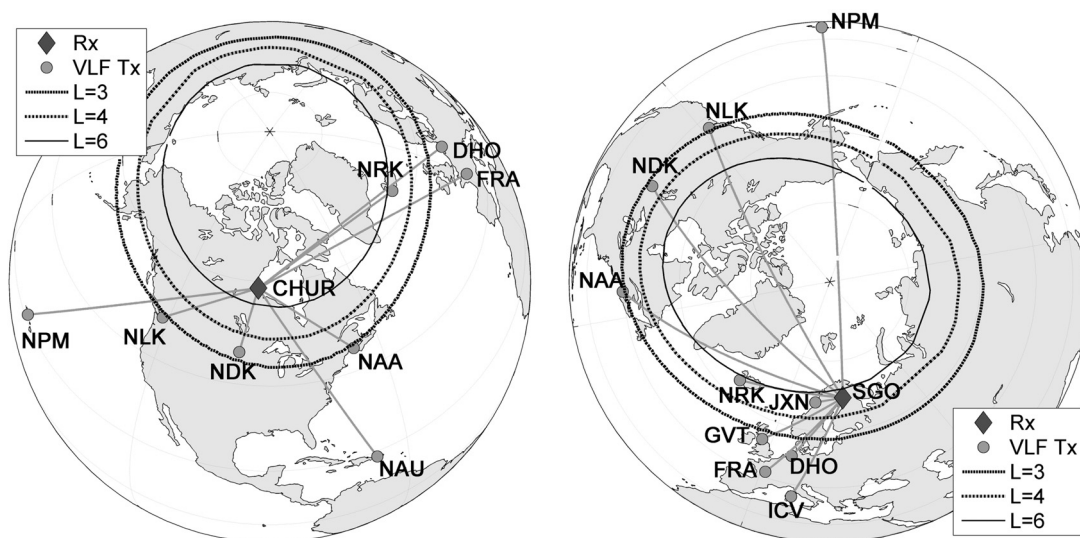


Figure 4. Map showing the AARDDVARK receivers at Churchill and Sodankylä (diamonds) and the VLF transmitters monitored by these receivers (circles). This map also indicates the great circle propagation paths between the transmitter and receiver, as well as a number of fixed L shell contours evaluated at 100 km altitude.

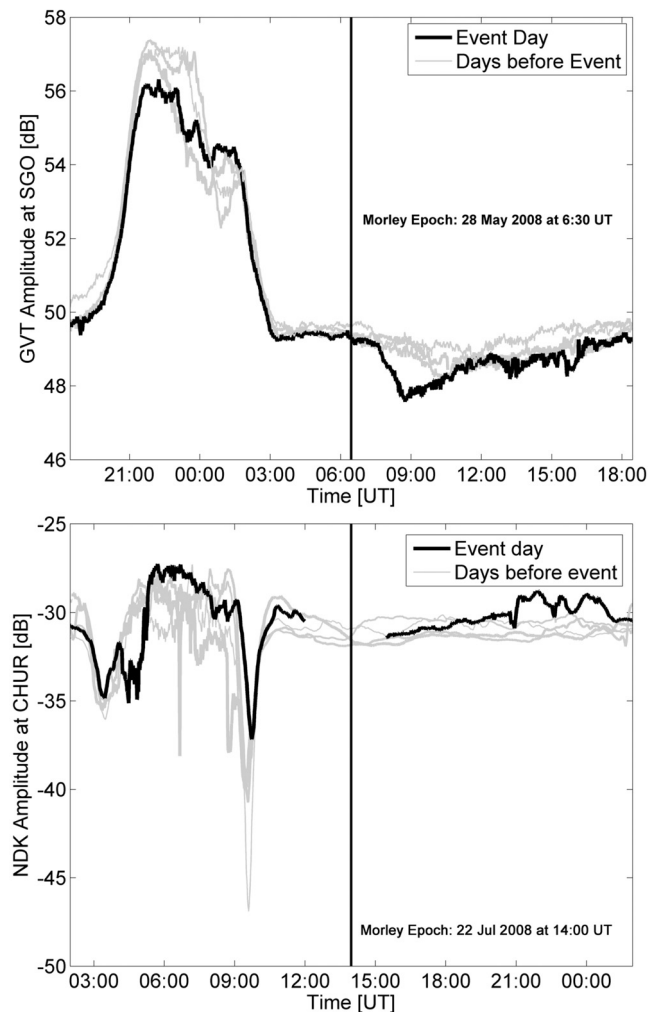


Figure 5. Examples of AARDDVARK observations made around the time of the Morley epochs (the epoch time is marked by the vertical lines in the center of the plots). Observations on the days before the epoch day are plotted in gray; the epoch day is in black. (top) GVT-Sodankylä amplitudes for the epoch at 6:30 UT on 28 May 2008. (bottom) NDK-Churchill amplitudes for the epoch at 14:00 UT on 22 July 2008.

decreases by ~ 1.3 dB, after which it returns to near-QDC levels. In the hours following, there are several subsequent examples of likely precipitation periods (i.e., ~ 13.5 and 15.5 UT), both of which have quite small amplitude changes in comparison with the first precipitation period.

The lower panel of Figure 5 presents the received amplitude of the NDK 25.2 kHz transmitter received at Churchill ($2.8 < L < 7.4$) around the Morley epoch at 14:00 UT on 22 July 2008. Once again, there is a long period when the entire path is sunlit, from ~ 12 to 02 UT. Unfortunately, the transmitter was not operating for a few hours around the time

of the epoch. However, the amplitude on the event day is well behaved from ~ 2 h after the epoch, showing a steady rise from 15.5 to 20.75 UT, followed by three broad bursts of precipitation at 21.5, 23, and 0.25 UT on the following day.

Of the 65 Morley epochs that we studied, there were 7 epochs for which there were no Sodankylä AARDDVARK observations either on the epoch day or on one of the days immediately before the epoch, leaving 58 epochs to examine. The Churchill AARDDVARK receiver was not installed until May 2007, halfway through the period containing the Morley epochs and was also not operating from December 2007 through May 2008. As a result, only 14 epochs were able to be examined in the Churchill data, although most of these epochs are also represented in Sodankylä observations. We classified data as showing evidence of EEP if an obvious deviation from the QDC could be seen concurrently on at least two different transmitter-receiver paths; this was to ensure the deviations we were seeing were, indeed, due to EEP, and not through random fluctuations in the AARDDVARK data.

We performed the above analysis on both the aforementioned Morley epochs. For the 67 Morley epochs, 2 epochs were removed due to solar proton activity, 4 were removed as neither receiver was operating, and 15 epochs were removed as there was no transmitter-receiver path with a good QDC. Of the remaining 46 epochs, 34 of these showed clear signs of EEP across multiple paths (i.e., 74%). This confirms the riometer- and satellite-based observations of significant EEP occurring during the SWSI dropouts and also provides us with an additional data set in order to determine the magnitude of the EEP entering the atmosphere.

5. AARDDVARK MODELING

For the next step, we returned to the Morley epochs, focusing on the paths that had a well-behaved QDC, again concentrating on times when the path is sunlit. We then focused on only three subionospheric transmitter-receiver paths; NAA 24.0 kHz to Churchill and GVT to Sodankylä, both of which are relatively short paths, which span a limited magnetic local time range, and the rather long path from NAA to Sodankylä. There is a significant amount of variability in the observed amplitude changes; this is hardly surprising given the large variability in the magnitude of the EEP from event to event evidenced from the interquartile range (not shown). However, we are still in a position to establish “typical” amplitude changes for the subionospheric VLF-observed SWSI-associated precipitation. These are shown in Table 1.

In order to determine the typical magnitude of the EEP triggered by the SWSI, we follow the modeling approach

Table 1. Summary of Ground-Based Instrument Responses During the SWSI-Triggered Geomagnetic Storms^a

| | Δ VLF obs. (dB) | Δ VLF calc. (dB) | Δ CNA calc. (dB) | EEP Flux |
|----------|------------------------|-------------------------|-------------------------|-----------------|
| NAA-CHUR | +2.0 | +2.0 | 1.41 | 1×10^6 |
| GVT-SGO | -1.5 | -1.1 | 1.05 | 4×10^5 |
| NAA-SGO | +2.5 | +2.5 | 1.35 | 9×10^5 |
| | Δ CNA obs. (dB) | Δ VLF calc. (dB) | Δ CNA calc. (dB) | EEP Flux |
| NAA-CHUR | 1.25 | +1.7 | 1.25 | 8×10^5 |
| GVT-SGO | 1.25 | -0.9 | 1.25 | 8×10^5 |
| NAA-SGO | 1.25 | +2.4 | 1.25 | 8×10^5 |

^aThe top half of the table examines the energetic electron precipitation (EEP) values necessary to best reproduce the subionospheric VLF observations from this study (Δ VLF obs.), while the lower half examines the EEP values necessary to best reproduce the *Morley et al.* [2010b]-reported riometer observations (Δ CNA obs.). In each case, the calculated change of the other ground-based instrument response is shown. The EEP values listed are >30 keV electron fluxes with units of electrons $\text{cm}^{-2} \text{sr}^{-1} \text{s}^{-1}$.

outlined in the work of *Rodger et al.* [2012]. Here our goal is to determine the fluxes, which will lead to the changes in VLF amplitude shown in Table 1. In addition, *Morley et al.* [2010b] reported that the SWSI-associated radiation belt dropouts were linked to increases in riometer-measured absorption of “cosmic noise,” which is expected due to increases in the ionization number density in the ionospheric D and E regions caused by EEP. A SEA of riometer data found that the change in cosmic noise absorption (Δ CNA) in Canadian and European instruments peaked at ~ 1.25 dB in the period 3–6 h following the epoch [*Morley et al.*, 2010b]. Thus, our modeling goal is to reproduce both the subionospheric VLF changes as well as those from the riometer SEA.

For each VLF transmitter-receiver path, we take a modeling point midway along the path and use a combination of International Reference Ionosphere (IRI-2007) [online from http://omniweb.gsfc.nasa.gov/vitmo/iri_vitmo.html] and typical D region electron-density profiles determined for high latitudes at noon [*Thomson et al.*, 2011]. We model the SWSI-associated EEP signature in ground-based data using 10 keV to 2.0 MeV precipitating electrons with an energy spectra determined by the POES SEA observations. During the peak precipitation period, the >30 , >100 , and >300 keV precipitating fluxes are best fitted terms of a power law where the slope (scaling exponent, k) is -3.5 . Otherwise, our modeling techniques follow that described by *Rodger et al.* [2012].

As shown in Table 1, a relatively small range of EEP flux magnitudes will reproduce the ground-based instrument responses observed during the SWSI-triggered geomagnetic storms. The top half of the table examines the EEP values necessary to best reproduce the subionospheric VLF amplitude change observations (Δ VLF obs.), and shows the predicted change in riometers absorption (Δ CNA calc.) predicted for that EEP flux striking the atmosphere at the midpoint of that path. Although the lower bound of the EEP

was assumed to be 10 keV (to more accurately capture the riometer responses), we report the >30 keV EEP flux magnitude to allow direct comparison with the POES 0° telescope observations, given below. Table 1 shows there is very good agreement between the modeled and predicted VLF responses (Δ VLF calc.) for the paths NAA-CHUR and NAA-SGO with >30 keV EEP flux magnitudes of $9\text{--}10 \times 10^5$ electrons $\text{cm}^{-2} \text{sr}^{-1} \text{s}^{-1}$ and slightly lower quality matching for the GVT-SGO path, where -1.1 dB is the largest negative amplitude change we can produce (compare, a typical change of -1.5 dB observed) for a >30 keV EEP flux magnitude of 4×10^5 electrons $\text{cm}^{-2} \text{sr}^{-1} \text{s}^{-1}$. These EEP are calculated to produce riometer absorption changes, which are similar to those reported (1–1.4 dB). The lower half of Table 1 examines the EEP values necessary to best reproduce the *Morley et al.* [2010b] reported peak riometer observations (Δ CNA obs. of 1.25 dB), and contrasts the Δ VLF calc. predicted for these fluxes. In all cases, despite the different undisturbed ionospheric electron density-height profiles and neutral atmospheric parameters, the typical observed Δ CNA is reproduced by an EEP flux magnitude of $\sim 8 \times 10^5$ electrons $\text{cm}^{-2} \text{sr}^{-1} \text{s}^{-1}$, with relatively small differences in the Δ VLF calc. relative to those observed.

6. DISCUSSION

The >30 keV EEP flux magnitude determined from Table 1 should be contrasted with that found in the SEA of the POES precipitating electrons. The peak in the median >30 keV POES 0° telescope fluxes is $\sim 7 \times 10^4$ electrons $\text{cm}^{-2} \text{sr}^{-1} \text{s}^{-1}$, with the 95% confidence interval for the median spanning $\sim 4 \times 10^4$ to 1×10^5 electrons $\text{cm}^{-2} \text{sr}^{-1} \text{s}^{-1}$. Clearly, this is approximately one order of magnitude smaller than the EEP determined in section 5 from the ground-based measurements. The difference is significant; if the EEP flux was 7×10^4 electrons $\text{cm}^{-2} \text{sr}^{-1} \text{s}^{-1}$, the riometer absorption change

would be only 0.27 dB. It is not unexpected that the POES-reported 0° telescope flux is a fraction of that in the bounce loss cone and striking the atmosphere. As noted in section 2.2, the POES SEM-2 0° telescope only samples a fraction of the loss cone, with 10% being a common “best case.”

Note that the typical SWSI-triggered >30 keV electron precipitation flux of 8×10^5 electrons $\text{cm}^{-2} \text{sr}^{-1} \text{s}^{-1}$ determined from the ground-based instruments should be considered a large electron precipitation event, although with a softer energy spectra than the $k = -2$ spectra reported as typical by Clilverd *et al.* [2010]. A >30 keV precipitation flux of 2.2×10^6 electrons $\text{cm}^{-2} \text{sr}^{-1} \text{s}^{-1}$ would occur if the entire electron flux stored in a $L = 6.5$ flux tube was precipitated out in a 10 min period, with the population calculated using the European Space Agency Space Environmental Effects-1 radiation belt model [Vampola, 1996]. In practice, the POES observations indicate that SWSI-triggered geomagnetic storm have roughly constant precipitation fluxes with values similar to those of the peak level for ~ 1.5 days. We speculate that this is evidence that the acceleration process, which “rebuilds” the energetic electron fluxes after the dropout, also produces electron precipitation, with a significant fraction of the accelerated electrons being lost into the atmosphere.

7. SUMMARY AND CONCLUSIONS

In this study, we have examined satellite- and ground-based observations to describe the significance of EEP during SWSI-driven geomagnetic storms, focusing on the Morley *et al.* [2010b] epochs to allow “like with like” comparisons with the earlier study focused primarily upon GPS observations. The SEA of the low-Earth-orbiting POES satellite observations confirm that SWSI-driven geomagnetic storms are strongly associated with large EEP events. However, the EEP only becomes significant at the time that the dropout is at its deepest point and is starting to recover, such that EEP cannot be used to explain the observed dropouts in trapped energetic radiation belt electrons for any energy range. Our observations are more suggestive of the opposite phenomena, where the EEP is the signature of wave-particle-driven acceleration processes, which serve to reverse the electron flux dropouts.

Previous studies have suggested that magnetopause shadowing may be the primary reason for the rapid dropouts. Our SEA is, however, not consistent with a simple model of direct magnetopause shadowing causing the losses. In particular, we found that the trapped proton fluxes increased rather than decreased during the dropouts, while the classic direct magnetopause shadowing explanation that would predict this mechanism would be independent of particle charge, mass, or energy, such that electrons or protons, which are

drifting around the Earth on the same L shell (but in opposite directions), will encounter the magnetopause and, hence, be lost.

Ground-based observation of subionospheric VLF propagation from the AARDDVARK network has been used to confirm the POES observations of large EEP events generated by the SWSI-triggered storms. For the epochs for which there were data available and well-defined QDCs, 74% of the Morley epochs showed evidence of EEP occurring, producing amplitude changes of several decibels. The EEP was observed typically ~ 3 h after the Morley epochs. The AARDDVARK observations were combined with riometer measurements made for the Morley *et al.* [2010b] epochs in order to model the magnitude of the EEP occurring in these events. The very high levels of agreement in the modeling, which involved multiple instruments, and multiple transmitter-receiver paths, indicates a strong probability that the >30 keV EEP flux magnitude has a value close to 8×10^5 electrons $\text{cm}^{-2} \text{sr}^{-1} \text{s}^{-1}$. This is ~ 11 times larger than the >30 keV EEP flux reported by the 0° directed >30 keV electron telescope measurements made onboard POES, which is expected as the POES telescopes only view $\sim 10\%$ of the bounce loss cone.

Acknowledgments. A.T.H., C.J.R., M.A.C., and N.R.T. were supported by the New Zealand Marsden Fund. The research leading to these results has also received funding from the European Union Seventh Framework Programme (FP7/2007-2013) under grant agreement 263218.

REFERENCES

- Clilverd, M. A., T. D. G. Clark, A. J. Smith, and N. R. Thomson (1993), Observation of a decrease in midlatitude whistler-mode signal occurrence prior to geomagnetic storms, *J. Atmos. Terr. Phys.*, *55*, 1479–1485, doi:10.1016/0021-9169(93)90113-D.
- Clilverd, M. A., et al. (2009), Remote sensing space weather events: Antarctic-Arctic Radiation-belt (Dynamic) Deposition-VLF Atmospheric Research Konsortium network, *Space Weather*, *7*, S04001, doi:10.1029/2008SW000412.
- Clilverd, M. A., C. J. Rodger, R. J. Gamble, T. Ulich, T. Raita, A. Seppälä, J. C. Green, N. R. Thomson, J.-A. Sauvaud, and M. Parrot (2010), Ground-based estimates of outer radiation belt energetic electron precipitation fluxes into the atmosphere, *J. Geophys. Res.*, *115*, A12304, doi:10.1029/2010JA015638.
- Evans, D. S., and M. S. Greer (2004), Polar orbiting environmental satellite space environment monitor – 2: Instrument descriptions and archive data documentation, *NOAA Tech. Memo. OAR SEC-93*, version 1.4, Space Environ. Lab., Boulder, Colo.
- Green, J. C., T. G. Onsager, T. P. O’Brien, and D. N. Baker (2004), Testing loss mechanisms capable of rapidly depleting relativistic electron flux in the Earth’s outer radiation belt, *J. Geophys. Res.*, *109*, A12211, doi:10.1029/2004JA010579.

- Hess, W. N. (1968), *The Radiation Belt and Magnetosphere*, Blaisdell, London, U. K.
- Lam, M. M., R. B. Horne, N. P. Meredith, S. A. Glauert, T. Moffat-Griffin, and J. C. Green (2010), Origin of energetic electron precipitation >30 keV into the atmosphere, *J. Geophys. Res.*, *115*, A00F08, doi:10.1029/2009JA014619.
- Loewe, C. A., and G. W. Prölss (1997), Classification and mean behavior of magnetic storms, *J. Geophys. Res.*, *102*(A7), 14,209–14,213, doi:10.1029/96JA04020.
- Meredith, N. P., R. B. Horne, M. M. Lam, M. H. Denton, J. E. Borovsky, and J. C. Green (2011), Energetic electron precipitation during high-speed solar wind stream driven storms, *J. Geophys. Res.*, *116*, A05223, doi:10.1029/2010JA016293.
- Miyoshi, Y., and R. Kataoka (2008), Flux enhancement of the outer radiation belt electrons after the arrival of stream interaction regions, *J. Geophys. Res.*, *113*, A03S09, doi:10.1029/2007JA012506.
- Morley, S. K., R. H. W. Friedel, T. E. Cayton, and E. Noveroske (2010a), A rapid, global and prolonged electron radiation belt dropout observed with the Global Positioning System constellation, *Geophys. Res. Lett.*, *37*, L06102, doi:10.1029/2010GL042772.
- Morley, S. K., R. H. W. Friedel, E. L. Spanswick, G. D. Reeves, J. T. Steinberg, J. Koller, T. Cayton, and E. Noveroske (2010b), Dropouts of the outer electron radiation belt in response to solar wind stream interfaces: Global positioning system observations, *Proc. R. Soc. A*, *466*(2123), 3329–3350, doi:10.1098/rspa.2010.0078.
- Newnham, D. A., P. J. Espy, M. A. Clilverd, C. J. Rodger, A. Seppälä, D. J. Maxfield, P. Hartogh, K. Holmén, and R. B. Horne (2011), Direct observations of nitric oxide produced by energetic electron precipitation into the Antarctic middle atmosphere, *Geophys. Res. Lett.*, *38*, L20104, doi:10.1029/2011GL048666.
- O'Brien, T. P., R. L. McPherron, D. Sornette, G. D. Reeves, R. Friedel, and H. J. Singer (2001), Which magnetic storms produce relativistic electrons at geosynchronous orbit?, *J. Geophys. Res.*, *106*(A8), 15,533–15,544.
- Reeves, G. D., K. L. McAdams, R. H. W. Friedel, and T. P. O'Brien (2003), Acceleration and loss of relativistic electrons during geomagnetic storms, *Geophys. Res. Lett.*, *30*(10), 1529, doi:10.1029/2002GL016513.
- Rodger, C. J., M. A. Clilverd, N. R. Thomson, R. J. Gamble, A. Seppälä, E. Turunen, N. P. Meredith, M. Parrot, J.-A. Sauvaud, and J.-J. Berthelier (2007), Radiation belt electron precipitation into the atmosphere: Recovery from a geomagnetic storm, *J. Geophys. Res.*, *112*, A11307, doi:10.1029/2007JA012383.
- Rodger, C. J., M. A. Clilverd, J. C. Green, and M. M. Lam (2010a), Use of POES SEM-2 observations to examine radiation belt dynamics and energetic electron precipitation into the atmosphere, *J. Geophys. Res.*, *115*, A04202, doi:10.1029/2008JA014023.
- Rodger, C. J., B. R. Carson, S. A. Cummer, R. J. Gamble, M. A. Clilverd, J. C. Green, J.-A. Sauvaud, M. Parrot, and J.-J. Berthelier (2010b), Contrasting the efficiency of radiation belt losses caused by ducted and nonducted whistler-mode waves from ground-based transmitters, *J. Geophys. Res.*, *115*, A12208, doi:10.1029/2010JA015880.
- Rodger, C. J., M. A. Clilverd, A. J. Kavanagh, C. E. J. Watt, P. T. Verronen, and T. Raita (2012), Contrasting the responses of three different ground-based instruments to energetic electron precipitation, *Radio Sci.*, *47*, RS2021, doi:10.1029/2011RS004971.
- Roederer, J. G. (1970), *Dynamics of Geomagnetically Trapped Radiation*, Springer, New York.
- Sandanger, M., F. Søråas, K. Aarsnes, K. Oksavik, and D. S. Evans (2007), Loss of relativistic electrons: Evidence for pitch angle scattering by electromagnetic ion cyclotron waves excited by unstable ring current protons, *J. Geophys. Res.*, *112*, A12213, doi:10.1029/2006JA012138.
- Seppälä, A., C. E. Randall, M. A. Clilverd, E. Rozanov, and C. J. Rodger (2009), Geomagnetic activity and polar surface air temperature variability, *J. Geophys. Res.*, *114*, A10312, doi:10.1029/2008JA014029.
- Thomson, N. R., C. J. Rodger, and M. A. Clilverd (2011), Daytime D region parameters from long-path VLF phase and amplitude, *J. Geophys. Res.*, *116*, A11305, doi:10.1029/2011JA016910.
- Thorne, R. M. (2010), Radiation belt dynamics: The importance of wave-particle interactions, *Geophys. Res. Lett.*, *37*, L22107, doi:10.1029/2010GL044990.
- Turner, D. L., S. K. Morley, Y. Miyoshi, B. Ni, and C.-L. Huang (2012), Outer radiation belt flux dropouts: Current understanding and unresolved questions, in *Dynamics of the Earth's Radiation Belts and Inner Magnetosphere*, *Geophys. Monogr. Ser.*, doi:10.1029/2012GM001310, this volume.
- Turunen, E., P. T. Verronen, A. Seppälä, C. J. Rodger, M. A. Clilverd, J. Tamminen, C. F. Enell, and T. Ulich (2009), Impact of different energies of precipitating particles on NO_x generation in the middle and upper atmosphere during geomagnetic storms, *J. Atmos. Sol. Terr. Phys.*, *71*, 1176–1189, doi:10.1016/j.jastp.2008.07.005.
- Vampola, A. L. (1996), Outer zone energetic electron environment update, *P.O. #151351*, Eur. Space Agency, Noordwijk, The Netherlands.
- Van Allen, J. A., and L. A. Frank (1959), Radiation measurements to 658,300 kilometers with Pioneer IV, *Nature*, *184*, 219–224.
- Yando, K., R. M. Millan, J. C. Green, and D. S. Evans (2011), A Monte Carlo simulation of the NOAA POES Medium Energy Proton and Electron Detector instrument, *J. Geophys. Res.*, *116*, A10231, doi:10.1029/2011JA016671.

M. A. Clilverd, British Antarctic Survey, High Cross, Madingley Road, Cambridge CB3 0ET, England, UK. (macl@bas.ac.uk)

A. T. Hendry, C. J. Rodger, and N. R. Thomson, Department of Physics, University of Otago, P.O. Box 56, Dunedin, New Zealand. (ahendry@physics.otago.ac.nz; crodger@physics.otago.ac.nz; n_thomson@physics.otago.ac.nz)

S. K. Morley, Los Alamos National Laboratory, Bikini Atoll Road, SM 30, Los Alamos, NM 87545, USA. (smorley@lanl.gov)

T. Raita, Sodankylä Geophysical Observatory, University of Oulu, Sodankylä, Finland. (tero.raita@sgo.fi)

